RSC Advances

PAPER

View Article Online
View Journal | View Issue

Check for updates

Cite this: *RSC Adv.*, 2020, **10**, 8460

Mechanism and activity of the oxygen reduction reaction on WTe_2 transition metal dichalcogenide with Te vacancy†

O My Na,[ab] Nguyen Thi Xuan Huynh,[abc] Pham Tan Thi,[ab] Viorel Chihaia[d] and Do Ngoc Son*[ab]

Received 23rd November 2019
Accepted 16th February 2020

DOI: 10.1039/c9ra09809g

rsc.li/rsc-advances

WTe_2 transition metal dichalcogenide is a promising candidate for the cathode of proton-exchange membrane fuel cells. In this paper, we investigated the mechanism and activity of the oxygen reduction reaction on the monolayer of the WTe_2 transition metal dichalcogenide with Te vacancy denoted as WTe_2^d. By using density functional theory calculations, we studied the reaction intermediates on the surface of WTe_2^d. The Gibbs free energy was calculated to clarify the thermodynamic properties of the reaction. We discovered that the ORR mechanisms are more favorable outside than inside the vacancy. The ORR activity was found to be comparable to that of the well-known transition metal electro-catalysts.

1. Introduction

In recent years, fuel cell technology has gradually shifted from basic research to practical application.[1] Proton exchange membrane fuel cells (PEMFCs) are one of the most promising candidates for renewable and sustainable energy conversion devices.[2] PEMFCs play a vital role in future energy systems for different purposes such as transportation, residential power generation, and portable computers.[3,4] However, the efficiency of PEMFCs is significantly influenced by slow kinetics of oxygen reduction reaction (ORR) at the cathode due to the difficulty to break the double bond of the oxygen molecules.[5,6] Researchers have studied various catalytic materials for the ORR to solve this problem.[7–9] Pt-based[10–16] and Pd-based alloys[17–20] have been extensively studied to replace the expensive Pt electro-catalyst. In many cases, ones found that the alloys improved not only the efficiency but also the durability of the cathode of the fuel cells.

Transition metal dichalcogenides (TMDs) have attracted our attention because they have been found in various applications,[21–26] in which TMDs are the promising catalysts for the oxygen reduction reaction.[26] The literature showed that the edge defects can enhance the rate of the ORR and enable the four-electron transfer mechanism on the defective MoS_2 in the acidic medium.[27] The Mo atoms at the edge of the MoS_2 nanosheets became the reactive sites for the adsorption of the O atoms, which improved the performance of the MoS_2 electro-catalyst toward the ORR.[28] The doping of MoS_2 by heteroatoms such as P, N, and O[29–31] was found to improve the adsorption strength of oxygen molecules and enhanced the ORR. Also, the Cu-doped MoS_2 exhibits moderate binding energy with the ORR intermediates and offers a better ORR activity than the other-metal doping.[32] The Vulcan XC-72R modified WS_2 nano-composite (WS_2/C) was expected to be a promising ORR catalyst for fuel cells.[33] The number of transferring electrons in the ORR is close to the four-electron process and the WS_2/C nano-composite exhibited superior electrochemical stability. The ORR catalytic activity of MoS_2/Fe-phthalocyanine hybrid nano-structures was also found to be excellent compared to that of the commercial Pt/C catalyst in pH 13 electrolyte, with a more positive half-wave potential (0.89 *vs.* 0.84 V), a smaller Tafel slope (35 *vs.* 87 mV dec^{-1}), and a much better durability (9.3% *vs.* 40% degradation after 20 h).[34] Furthermore, the hetero-structures of (MoS_2, $MoSe_2$, WSe_2)/graphene and carbon nano-sheet were demonstrated to facilitate the ORR with the more positive onset potentials and higher kinetic current densities.[35–37] Recently, Liu *et al.* reported the influence of oxidation on the structure and electronic properties of monolayer TMD.[38] They showed that the perfect monolayer TMDs are almost inert to O_2 molecules while the defective monolayer TMDs can adsorb O_2 with the adsorption energy of about −1.8 to −3.9 eV. Interestingly, after the adsorption, the dissociation of O_2 on the monolayer WTe_2^d does not require activation energy. Based on these properties, we expect that the monolayer WTe_2^d can be a suitable catalytic material for the ORR.

In this work, we reported on the mechanism and activity of the ORR on the Te defective WTe_2 structure, which has never studied previously, by using the density functional theory

[a]Ho Chi Minh City University of Technology (HCMUT), Ho Chi Minh City, Vietnam. E-mail: dnson@hcmut.edu.vn

[b]Vietnam National University, Ho Chi Minh City, Vietnam

[c]Quy Nhon University, Binh Dinh Province, Vietnam

[d]Institude of Physical Chemistry "Ilie Murgulescu" of the Romanian Academy, Splaiul Independentei 202, Sector 6, 060021 Bucharest, Romania

† Electronic supplementary information (ESI) available. See DOI: 10.1039/c9ra09809g

calculations in combination with a thermodynamic model. We explored the possible ORR intermediates in different surface regions of WTe_2^d. The ORR mechanisms were proposed and then the Gibbs free energy diagrams were built. The results pointed out that the best performance of the ORR was obtained on the perfect region and the boundary with the defect region on the surface of WTe_2^d.

2. The computational methods

The calculations were carried out with the Vienna *ab initio* simulation package in the framework of density functional theory (DFT).[39] We used the plane-wave basis set with the kinetic energy cut-off of 600 eV. The general gradient approximation of Perdew–Burke–Ernzerhof was used for exchange-correlation functional.[40,41] The core-valence interaction was simulated by the projector augmented wave method.[42–44] The Brillouin zone integration was done with the sampling technique of Monkhorst and Pack,[45] in which the *k*-point mesh of 3 × 3 × 1 was selected. In this work, we used the dipole corrections for periodic supercells. To support the convergence of the calculations, we used the Methfessel-Paxton smearing of order 1 with the sigma value of 0.1 for the atomic position optimization and the linear tetrahedron method with Blöchl corrections for the total energy. The unit cell of WTe_2^d (see Fig. 1a) was constructed by removing one Te atom from the surface of the perfect WTe_2 unit cell. The unit cell has a hexagonal structure with the dimensions: $a = b = 17.61$ Å, $c = 16.00$ Å, the lattice parameter of 3.52 Å, and the vacuum space of about 13 Å. The unit cell size is large enough so that the creation of the vacancy of 1/25 ML from the perfect structure does not cause strain effect on the WTe_2^d. The atomic positions of WTe_2^d were fully relaxed during performing geometric optimization. We ignored the solvent effects in this study. Also, the reaction intermediates were investigated at a specific coverage. The effects of surface coverages will be considered in future studies.

The interactions between the ORR intermediates and WTe_2^d were quantified through the adsorption energy,

$$E_{ads} = E_{total} - (E_{sub} + E_{int}), \quad (1)$$

where E_{total}, E_{sub}, and E_{int} are the total energy of the following systems: WTe_2^d + ORR intermediate, the isolated WTe_2^d, and the isolated ORR intermediate, respectively.

We used the nudged elastic band (NEB) and climbing image NEB (CI-NEB) methods[46–48] to investigate the minimum energy pathway (MEP) of the O_2 dissociation process on the surface of the defective monolayer WTe_2.

The Gibbs free energy was calculated to understand the thermodynamic properties of the ORR intermediate steps,[49]

$$\Delta G = \Delta E + \Delta ZPE - T\Delta S, \quad (2)$$

where ΔE, ΔZPE, and ΔS are the intermediate reaction energy, the vibrational energy difference, and the entropy change for gas-phase molecules, respectively. ΔE and ΔZPE were estimated from the results of the DFT calculations, and ΔS was taken from ref. 49. In the present work, we considered the free energy at the equilibrium potential of 1.23 V, the standard atmospheric pressure of 1 bar, the room temperature of 300 K, and the pH is zero. The Gibbs free energy at pH = 0 with electrode potential corrections is:

$$\Delta G(U) = \Delta G + eU. \quad (3)$$

3. Results and discussion

We searched for the ORR intermediates by (i) loading the molecular and atomic oxygen on the defective WTe_2 monolayer, (ii) then successively loading the hydrogen atoms over the molecular and atomic oxygen and the previously formed intermediates, and (iii) finally optimizing the obtained structures in steps (i) and then (ii). The stable ORR intermediates are those with negative adsorption energy, which was calculated by using eqn (1).

Atomic oxygen adsorption (O*)

The asterisk denotes the adsorption state of the atomic oxygen on the surface of the substrate. The adsorption was investigated on three regions of the WTe_2^d substrate, see Fig. 1b, which are:

- Above the defect (region I);
- Inside the defect (region II); and
- Outside the defect or on the perfect region (region III).

We found three favorable adsorption sites of the atomic oxygen as presented in Fig. 2. The atomic oxygen adsorbs in the boundary of regions II and III denoted as the boundary II–III (Fig. 2a), region II (Fig. 2b), and region III (Fig. 2c). Interestingly,

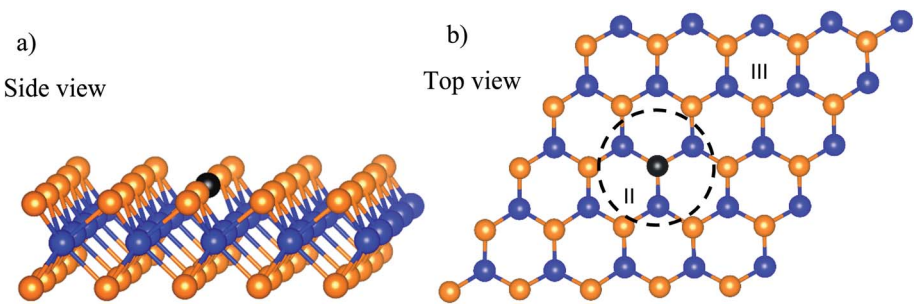

Fig. 1 The unit cell of the defective monolayer WTe_2. The blue and orange spheres represent the W and Te atoms, respectively. The black-solid point marks the position of the Te vacancy.

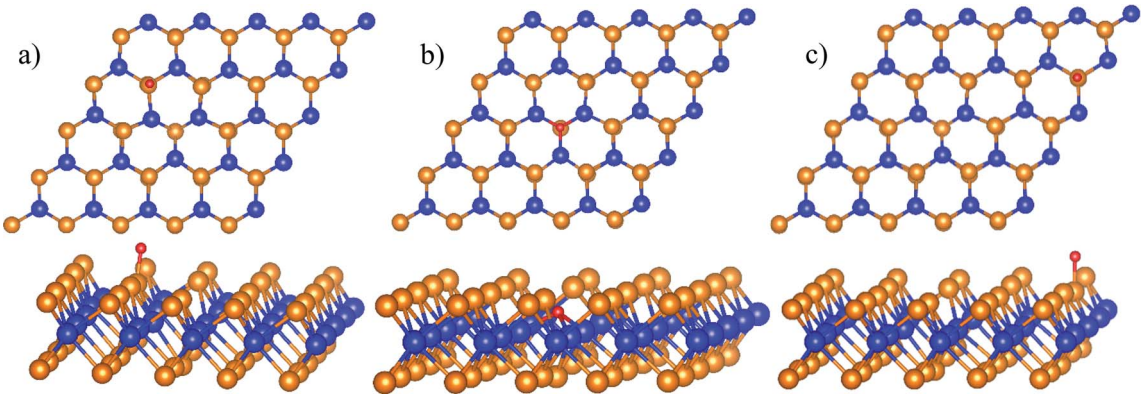

Fig. 2 The most stable structures of the atomic oxygen in each surface region of WTe_2^d: boundary II–III (a), region II (b), and region III (c). The spheres are W (blue), Te (orange), and O (red). The upper and lower panels are the top and side views, respectively.

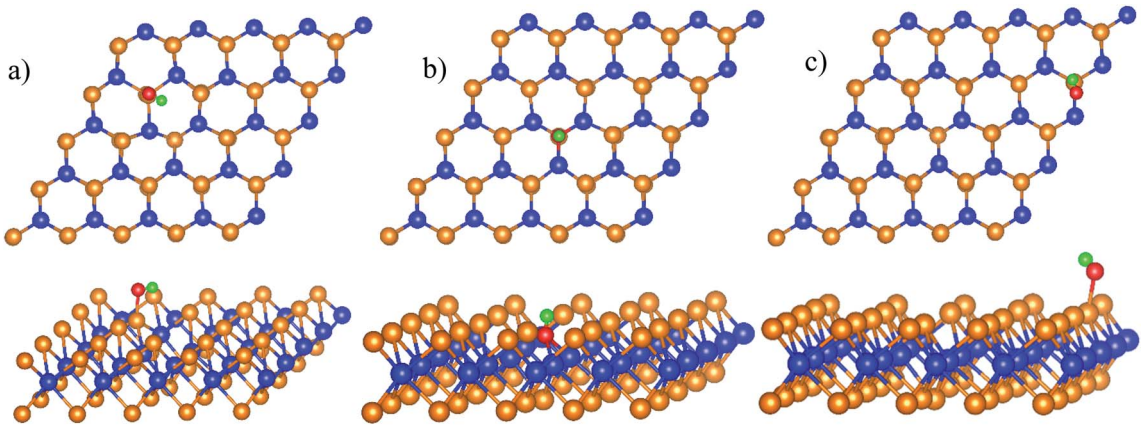

Fig. 3 The most stable structures of HO* in each region of WTe_2^d: boundary II–III (a), region II (b), and region III (c). The spheres are W (blue), Te (orange), O (red), and H (green). The upper and lower panels are the top and side views, respectively.

the adsorption energy of −0.59 eV and the distance between the O atom and the nearest Te atom is 1.85 Å in the boundary II–III are the same as those in region III. In region II, the atomic oxygen adsorbs strongly with the adsorption energy of −4.93 eV. The position of the O atom is at the center of the defect (see Fig. 2b), where the distance from the O atom to the nearest Te and W atoms is 3.51 Å and 2.08 Å, respectively.

HO* adsorption

The total energy of the isolated HO is −7.761 eV, which was used for the calculation of HO* adsorption energy. The favorable adsorption configurations are shown in Fig. 3.

Table 1 shows that the adsorption strength of HO* follows the order: region II > boundary II–III > region III. The distance from the O* atom to the nearest Te and W atoms is 2.0 and 4.0 Å for the boundary and region III; and is 3.4 Å and 2 Å for region II, respectively.

Table 1 The adsorption energy (eV) of O* and HO* on the WTe_2^d substrate

Intermediate	Boundary II–III	Region II	Region III
O*	0.59	−4.93	−0.59
HO*	−1.82	−4.24	−1.68

Molecular oxygen adsorption (O_2^*)

Initially, the oxygen molecule was arranged in different configurations, *i.e.*, the bond of two oxygen atoms is

Table 2 The adsorption energy of O_2^* on the WTe_2^d substrate and the distances between two oxygen atoms (d_{O-O}), from the nearest oxygen atom to the nearest tellurium atom (d_{O-Te}), and the nearest oxygen atom to the nearest tungsten atom (d_{O-W})

	Structure	Adsorption energy (eV)	d_{O-O} (Å)	d_{O-Te} (Å)	d_{O-W} (Å)
Region I	**D1**	**−0.63**	**1.24**	**3.40**	**4.72**
	D3	−0.25	1.24	4.25	4.93
Region II	**D2**	**−3.25**	**1.52**	**2.90**	**2.04**
	D4	−2.62	1.46	3.46	2.16
Region III	**P1**	**−0.60**	**1.24**	**3.35**	**3.54**
	P2	−0.58	1.26	3.60	5.21
	P3	−0.56	1.24	3.23	4.62

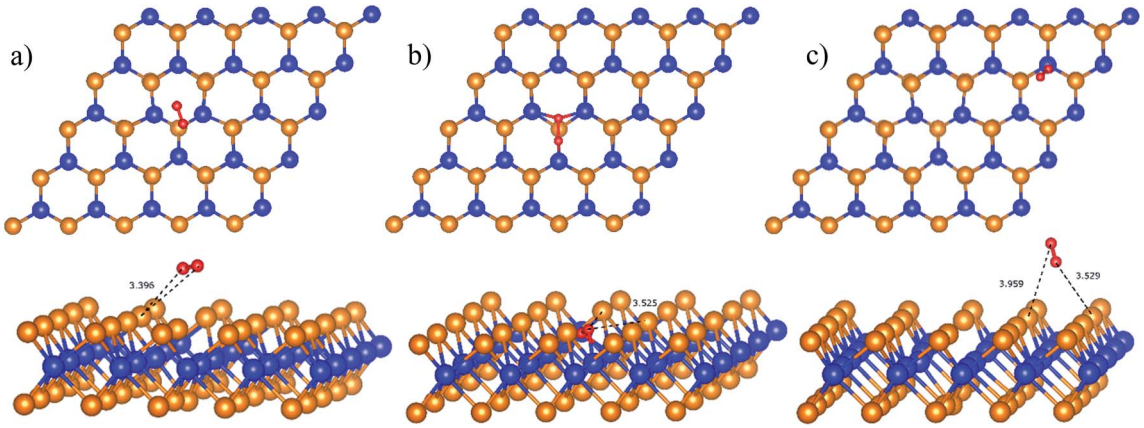

Fig. 4 The most favorable adsorption sites of the molecular oxygen on WTe_2^d: D1 in region I (a), D2 in region II (b), and P1 in region III (c). The spheres are W (blue), Te (orange), and O (red). The upper and lower panels are the top and side views, respectively.

perpendicular to, parallel to, and tilted with the surface of WTe_2^d. After performing the structure optimization of the initial configurations in each surface region of the unit cell, we calculated the adsorption energy of O_2^*, which is listed in Table 2. For the isolated oxygen molecule, the total energy was obtained to be −9.871 eV and the bond distance of two oxygen atoms is 1.23 Å. The favorable adsorption configurations are D1, D2, and P1 as presented in Fig. 4; and the less favorable configurations are D3, D4, P2, and P3 as shown in Fig. S1 in ESI.† Where, the name of each configuration enclosed with the letters D and P for the defect and perfect regions, respectively.

Because of the more negative adsorption energy, the most favorable adsorption of O_2^* for the regions I, II, and III were found to be D1, D2, and P1, respectively. Table 2 also shows that the adsorption energy of O_2^* in the regions I and II is approximately the same, but greatly different compared to that of region II, because O_2^* is in the molecular and atomic state for the former and latter, respectively. We can understand the differences in the states of O_2^* and the structures of D1, D2, and P1 by analyzing their structural parameters, which are listed in Table 2. We find that the bond length between two oxygen atoms is the same for O_2^* in the regions I and III; however, the bond length is significantly longer by 0.28 Å as O_2^* in region II. The configuration with the longer d_{O-O} bond length has the shorter d_{O-W} and d_{O-Te} distances. This result implies that when the oxygen molecule comes closer to the surface, the adsorption becomes stronger and therefore the distance of the two oxygen atoms becomes elongated; and hence, the oxygen atoms gradually moves far from one another. The distance between two oxygen atoms in the region II longer by 0.28 Å compared to that in the region I and III were also found to be in good agreement with the result in the literature.[38]

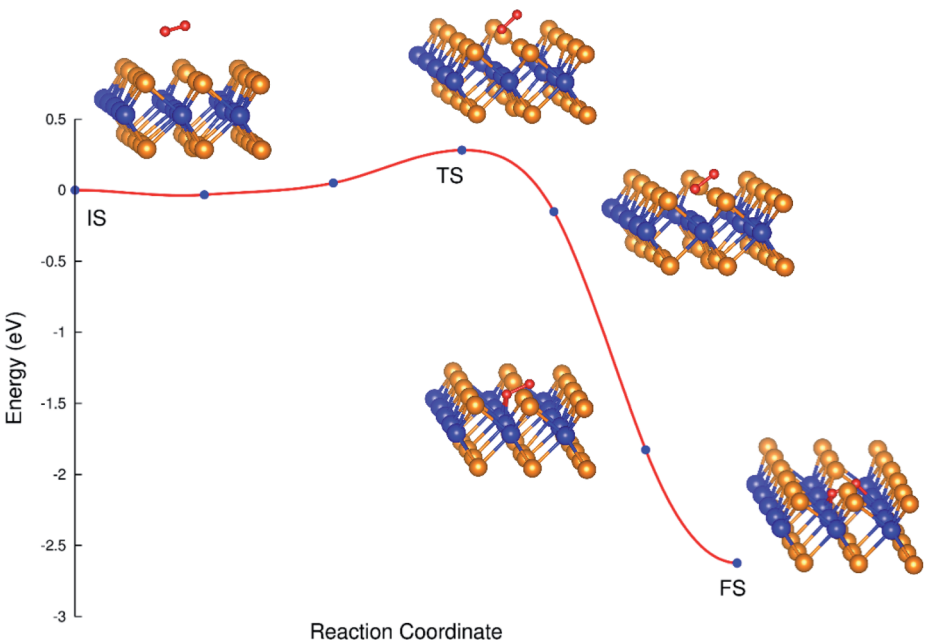

Fig. 5 The MEP from the initial to final state.

Table 3 The bond distances between the atoms in the NEB images from the IS to FS

	IS	01	02	FS	04	05	FS
$d_{(O-O)}$ (Å)	1.24	1.24	1.25	1.28	1.40	1.48	1.52
$d_{(O-W)}$ (Å)	4.72	4.26	3.59	2.76	2.25	2.15	2.04
$d_{(O-Te)}$ (Å)	3.40	3.53	3.30	2.98	2.90	2.90	2.90

MEP and CI-NEB results

The transition from D1 to D2 is possible. We have to use the NEB and CI-NEB techniques to search for the MEP and understand the transition. The configuration D1 and D2 are considered as the initial state (IS) and final state (FS) of the transition process, respectively.

Fig. 5 shows the minimum energy reaction path, where the saddle point (TS) is higher than the IS point by 0.28 eV, which implies that the transition from the initial to the final state requires the activation energy of 0.28 eV. This result is different compared to the case found in ref. 38, where the transition takes place automatically. This difference may be due to the influence of van der Waals interaction, which has been included in the previous work.[38] The final state is rather stable due to its lower energy. The energy difference between the saddle point and the FS point is 2.26 eV, which is rather large; and therefore, the transition from D1 and D2 is almost irreversible without providing a reasonable amount of energy.

Table 3 shows the varying tendency of the bond distances from the IS to FS. The bond length of the oxygen atoms increases, while the distances from the nearest oxygen atom to the tellurium and tungsten atoms decrease.

The charge density difference of the $O_2^* + WTe_2^d$ system in the initial and final states in Fig. 6 shows that the oxygen atoms are the centers of charge gain. The charge-gain cloud covers both oxygen atoms in the initial state, while it is well separated to each oxygen atom in the final state. This result indicates that the oxygen atoms are in the molecular and atomic states for the initial and final states, respectively. The

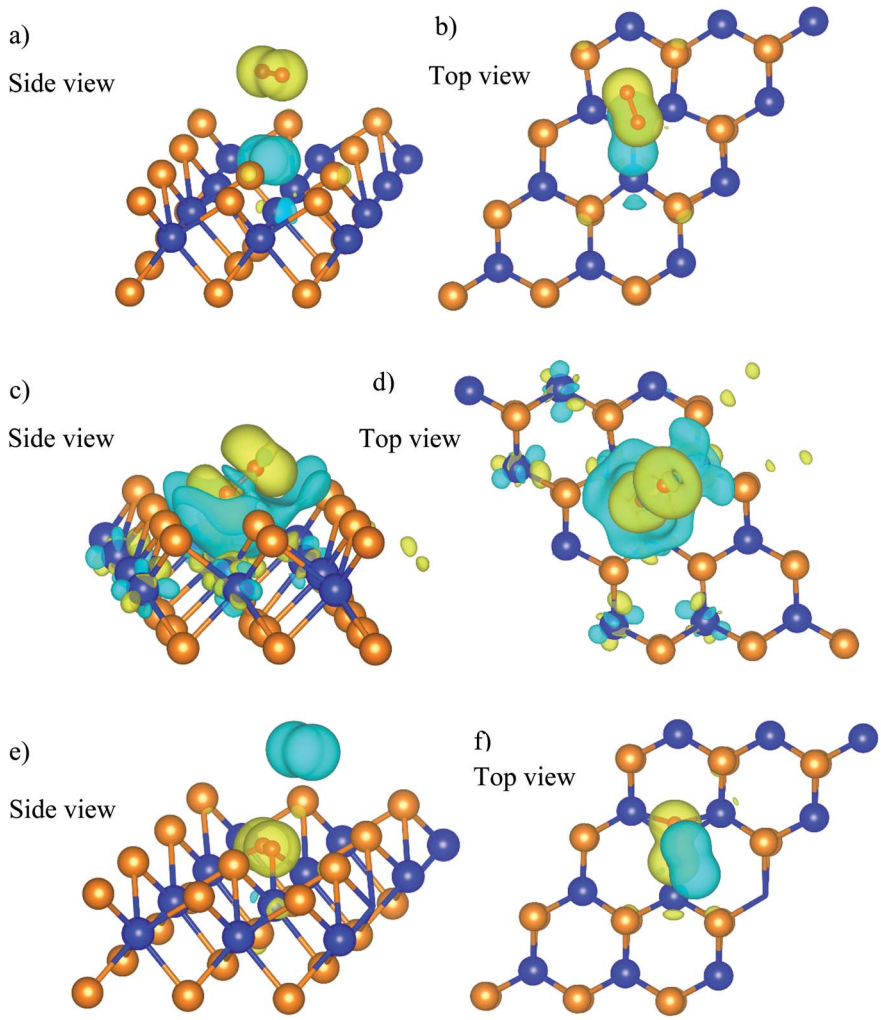

Fig. 6 The charge density difference of the $O_2^* + WTe_2^d$ system in the initial (a and b), transition (c and d), and final (e and f) states. The yellow and cyan clouds indicate the charge gain and loss, respectively.

Table 4 The adsorption energy (eV) of HOO*/HO* + O* and HOOH*/HO* + HO* on WTe_2^d

Intermediate	Region I	Region II	Region III
HOO*/HO* + O*	−0.75 (D11)[a]	−5.19 (D21)[b]	−0.75 (P11)[a]
HOOH*/HO* + HO*	−0.72 (D112)[c]	−5.77 (D212)[d]	−0.69 (P112)[c]

[a] HOO*. [b] HO* + O*. [c] HOOH*. [d] HO* + HO*.

charge increase of the oxygen atoms as compared to that of the neutral ones is 0.075, 0.44, and 1.703 e^- for the IS, TS, and FS, respectively.

First proton transfer process

We performed the first proton transfer process by loading a hydrogen atom over the adsorbed oxygen atoms in the configurations D1, D2, and P1. We obtained the optimized structure of HOO* and HO* + O* intermediates on the substrate surface. The structure of HO* + O* was obtained by loading and optimizing a hydrogen atom on the top and around the O* + O* intermediate in the structure D2. The isolated HOO has a total energy of −13.263 eV and the distance between the atoms is $d_{H-O} = 0.99$ Å and $d_{O-O} = 1.35$ Å. The isolated HO and O have the total energy of $E_{HO} = -7.76$ eV and $E_O = -4.94$ eV, respectively. The adsorption energy of HOO* and HO* + O* are listed in Table 4 and the optimization structures D11, D21, and P11 are presented in Fig. 7.

The configuration D21 is different compared to D11 and P11, see Fig. 7. Here, the reaction intermediate in D21 is HO* + O* with $d_{O-O} = 2.30$ Å. While the intermediate in D11 and P11 is HOO* with the distance $d_{O-O} = 1.36$ Å. The bond distances of the oxygen atoms are also found to be longer as compared with that of O_2^*. Besides, the adsorption energy for the D21 configuration is much lower than that of D11 and P11, see Table 4. The second proton transfer process will be carried out by using the D11, D21, and P11 configurations as the initial structures.

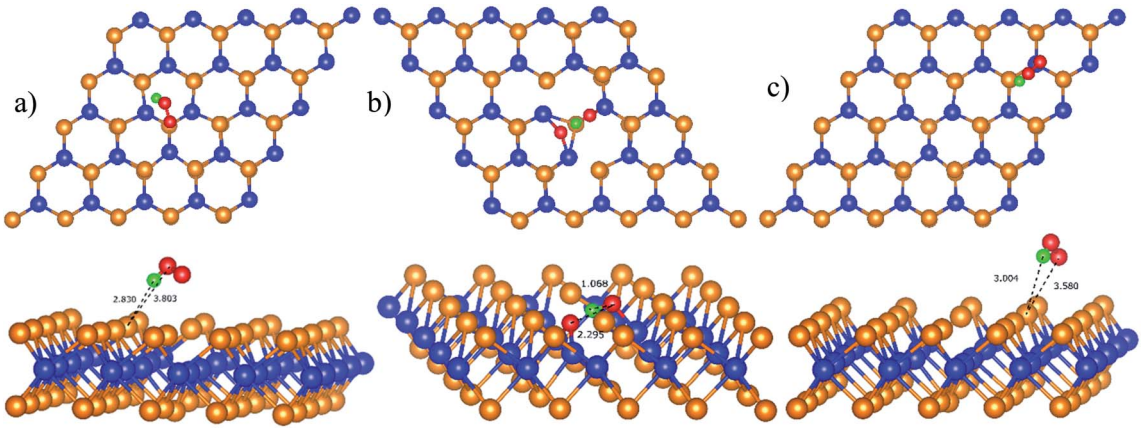

Fig. 7 The most stable configuration of HOO* is D11 (a) and P11 (c); and that of HO* + O* is D21 (b). The spheres are W (blue), Te (orange), O (red), and H (green). The upper and lower panels are the top and side views, respectively.

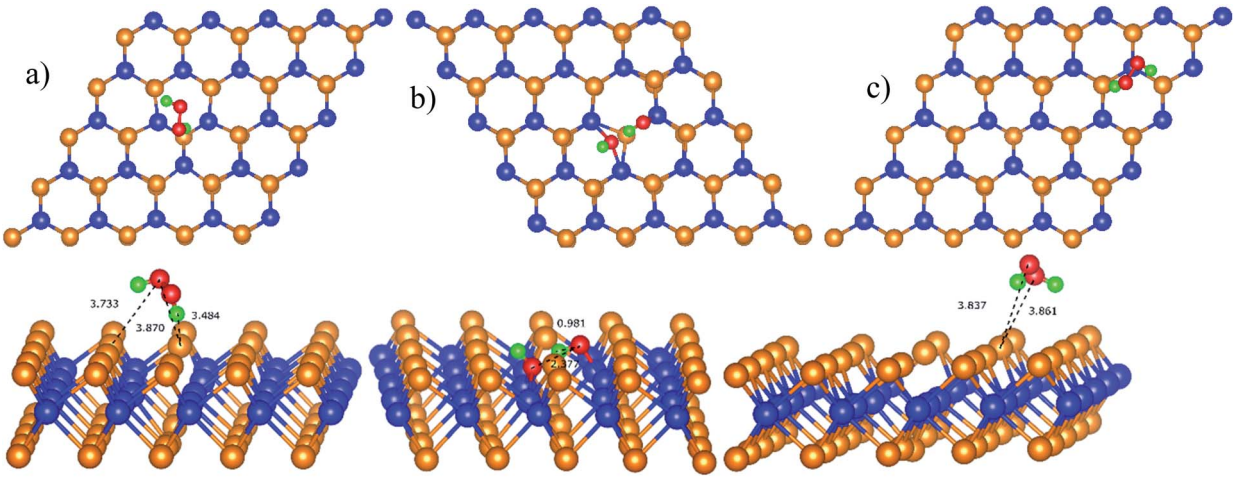

Fig. 8 The most stable structure of HOOH* is D112 (a) and P112 (c); and that of HO* + HO* is D212 (b). The spheres are W (blue), Te (orange), O (red), and H (green). The upper and lower panels are the top and side views, respectively.

Second proton transfer process

Similar to the case of the first proton transfer process, we found the most favorable intermediates based on the calculated adsorption energy (Table 4), where the total energy of the isolated HOOH is −18.15 eV. Fig. 8 shows that the intermediates of the second proton transfer process are HOOH* and HO* + HO*. The bond distance of the oxygen atoms slightly increases by around 0.1 Å compared to that of the corresponding previous intermediates of the first proton transfer process.

Reaction mechanism

There are two possible mechanisms for the oxygen reduction reaction. The dissociative one occurs as follows:

$$\frac{1}{2}O_2 + * \rightarrow O^*, \tag{4}$$

$$O^* + H^+ + e^- \rightarrow HO^*, \tag{5}$$

$$HO^* + H^+ + e^- \rightarrow H_2O + *. \tag{6}$$

The associative mechanism proceeds by:

$$O_2 + * \rightarrow O_2^*, \tag{7}$$

$$O_2^* + (H^+ + e^-) \rightarrow HOO^*, \tag{8}$$

$$HOO^* \rightarrow HO^* + O^*, \tag{9}$$

$$HOO^* + (H^+ + e^-) \rightarrow HOOH^*, \tag{10}$$

$$HO^* + O^* + (H^+ + e^-) \rightarrow H_2O + O^*, \tag{11}$$

$$HO^* + O^* + (H^+ + e^-) \rightarrow HO^* + HO^*, \tag{12}$$

$$HOOH^* + (H^+ + e^-) \rightarrow HO^* + H_2O, \tag{13}$$

$$O^* + H^+ + e^- \rightarrow HO^*, \tag{14}$$

$$HO^* + H^+ + e^- \rightarrow H_2O. \tag{15}$$

where * represents for the adsorption state of the intermediates on WTe_2^d. The eqn (14) and (15) are the same as (5) and (6).

Gibbs free energy

We can understand the thermodynamics of the ORR mechanism through the study of Gibbs free energy diagrams. We first performed the zero-point energy (ZPE) calculations. Table 5 shows the results of the ZPE of the intermediates for each region of the substrate surface.

The expressions for the Gibbs free energy of each mechanism are presented in the following part.[49–52] For the dissociative mechanism:

$$\Delta G_0(U) = G_{H_2O}(U) - G_{O^*+H_2}(U) = \Delta G_0(0) + eU, \tag{16}$$

$$\Delta G_1(U) = G_{HO^*+\left(\frac{1}{2}\right)H_2}(U) - G_{O^*+H_2}(U) = \Delta G_1(0) + eU, \tag{17}$$

$$\Delta G_2(U) = G_{H_2O}(U) - G_{HO^*+\left(\frac{1}{2}\right)H_2}(U) = \Delta G_2(0) + eU. \tag{18}$$

For the associative mechanism.

$$\Delta G_0(U) = G_{2H_2O}(U) - G_{O_2^*+2H_2}(U) = \Delta G_0(0) + eU, \tag{19}$$

$$\Delta G_1(U) = G_{O_2^*+2H_2}(U) - G_{HOO^*+\frac{3}{2}H_2} = \Delta G_1(0) + eU, \tag{20}$$

$$\Delta G_2(U) = G_{2H_2O}(U) - G_{HOO^*+\frac{3}{2}H_2}(U) = \Delta G_2(0) + eU, \tag{21}$$

$$\Delta G_3(U) = G_{2H_2O}(U) - G_{HO^*+O^*+\frac{3}{2}H_2}(U) = \Delta G_3(0) + eU, \tag{22}$$

$$\Delta G_4(U) = G_{2H_2O}(U) - G_{HOOH^*+H_2}(U) = \Delta G_4(0) + eU \tag{23}$$

$$\Delta G_5(U) = G_{2H_2O}(U) - G_{HO^*+HO^*+H_2}(U) = \Delta G_5(0) + eU, \tag{24}$$

$$\Delta G_6(U) = G_{2H_2O}(U) - G_{O^*+H_2O+H_2}(U) = \Delta G_6(0) + eU. \tag{25}$$

The results of Gibbs free energy are listed in Table 6 and 7; and the Gibbs free energy diagrams for the dissociative and associative mechanisms are presented in Fig. 9, 10 and 11, respectively.

Three intermediate steps involved in the dissociative mechanism for the conversion from $\frac{1}{2}O_2 + (H^+ + e^-)$ to H_2O, which includes the adsorption of atomic oxygen and two hydrogenation steps. Fig. 9 shows that after O* absorbed on the substrate, the first and second hydrogenation steps occur to convert O* to HO*, and HO* to H_2O, respectively. Noticeably, the adsorption of O* is downhill, and hence O* easily form on the surface of the substrate; however, the first hydrogenation step has to overcome an energy barrier of 2.81 eV for region II and about 0.95 eV for the boundary II–III and region III. Furthermore, for region II, the energy level of the HO* formation step is below that of H_2O, which causes the reverse reaction of forming HO* from H_2O automatically. Whilst, there are no reverse reactions in the

Table 5 The zero-point energy (eV) of the ORR intermediates

Intermediate	Boundary II–III	Region II	Region III
O*	0.058	0.086	0.061
HO*	0.333	0.364	0.312
O_2*/2O*	0.105 **(region I)**	0.147	0.098
HOO*/HO* + O*	0.409 **(region I)**	0.421	0.389
2HO*/HOOH*	0.715 **(region I)**	0.766	0.718

Table 6 Gibbs free energy for the intermediate reaction steps in the dissociative mechanism

	Gibbs free energy (eV) at $U = 1.23$ V		
Active sites	$\Delta G_0(U)$	$\Delta G_1(U)$	$\Delta G_2(U)$
Boundary II–III	0.494	0.883	−0.389
Region II	4.806	2.811	1.995
Region III	0.492	0.998	−0.506

Table 7 Gibbs free energy for the intermediate reaction steps in the associative mechanism

	Gibbs free energy (eV) at $U = 1.23$ V						
Active sites	$\Delta G_0(U)$	$\Delta G_1(U)$	$\Delta G_2(U)$	$\Delta G_3(U)$	$\Delta G_4(U)$	$\Delta G_5(U)$	$\Delta G_6(U)$
Region I	0.442	−1.451	−1.009	—	−1.124	—	
Region II	3.023	—	—	2.850		1.255	2.019
Region III	0.424	−1.411	−0.987	—	−0.830	—	

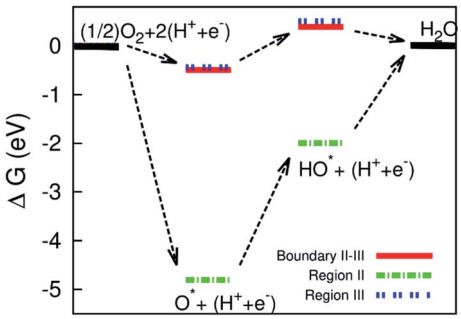

Fig. 9 Gibbs free energy diagram for the dissociative mechanism on the surface of the defective WTe_2.

boundary II–III and region III. The reverse reaction makes the ORR more difficult to maintain the byproduct H_2O and hence lower the efficiency of the fuel cells. We found that the formation of H_2O requires significantly smaller activation energy, *i.e.*, 0.95 eV in the boundary II–III and region III compared to 4.81 eV in region II. The characteristics of the Gibbs free energy diagram for the dissociative mechanism on the defective WTe_2 were found to be similar to that on the transition alloys.[50]

Fig. 10 and 11 show the Gibbs free energy diagrams for the associative mechanism. For regions I and III, the adsorption of O_2^* occurs automatically. However, the formation of HOO* and HOOH* requires the activation energy of 1.41 and 1.52 eV counted from the energy level of O_2^*, respectively. The rate-limiting step is the first hydrogenation process for region III and the second hydrogenation process forming HOOH* for region I. We find that the ORR proceeds to form H_2O more easily on region III than on region I. The reverse ORR does not automatically happen on these surface regions of the substrate.

The diagram in Fig. 11 is different compared to that in Fig. 10. This diagram was constructed from the combination between the NEB result and Gibbs free energy. The energy for the IS, TS, and FS structures of the O_2^* dissociation process was calculated with the inclusion of the electrode potential, ZPE, and entropy. The O_2 molecule adsorbs in region I to form $O_2^* + 4(H^+ + e^-)$, then overcome the energy barrier of 0.28 eV to create 2O* + 4 $(H^+ + e^-)$. The first hydrogenation step converts this intermediate to HO* + O* + 3$(H^+ + e^-)$. The second hydrogenation step transforms HO* + O* + 3 $(H^+ + e^-)$ into HO* + HO* + 2 $(H^+ + e^-)$ and O* + H_2O + 2 $(H^+ + e^-)$. The hydrogenation steps are uphill; therefore, absorb energy to proceed with the reaction. The energy consumption is about 3 eV to completely transform the intermediates into the final product of $2H_2O$. Noticeably, the reverse reaction perhaps occurs in this case. Therefore, one can not maintain the final product without continuously supplying the energy for the reaction. We can see that the Gibbs free energy in eqn (2) includes the reaction energy ΔE, $\Delta E = E_{(\text{after reaction})} - E_{(\text{before reaction})}$. The NEB energy barrier ΔE_{NEB} is similar to ΔE, $\Delta E_{\text{NEB}} = E_{(\text{saddle point})} - E_{(\text{before reaction})}$. Therefore, we can apply the same expressions for the Gibbs free energy to the saddle point by substituting ΔE_{NEB} for ΔE. Whilst the other parameters in eqn (2) can be calculated in the same manner as those for the intermediate reactions.

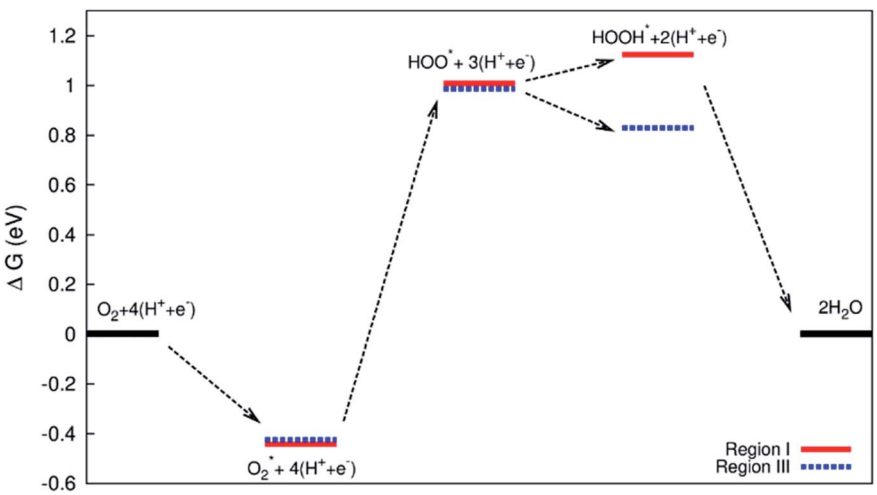

Fig. 10 Gibbs free energy diagram for the associative mechanism in regions I and III.

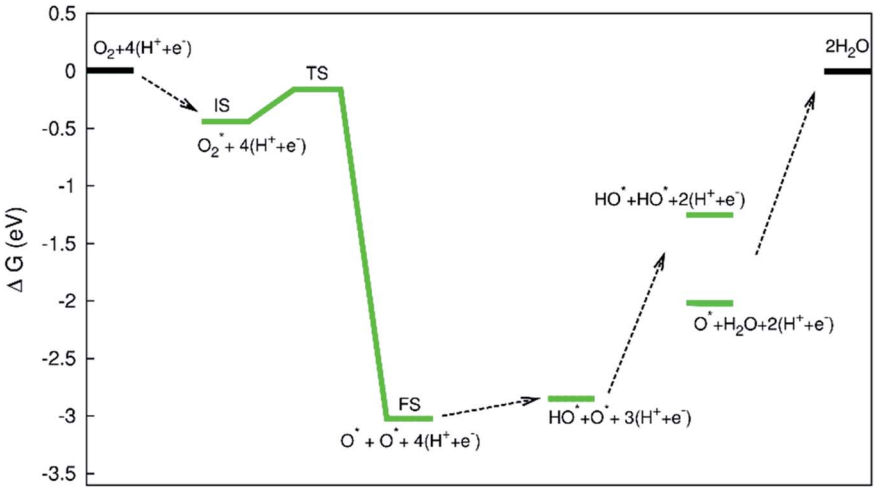

Fig. 11 Gibbs free energy diagram for the associative mechanism in region II.

Therefore, the combination of Gibbs and NEB calculations can display a more complete picture of the reaction including also the transition point.

From the above results, we realize that the Te defective monolayer WTe_2 can provide excellent active sites for the oxygen reduction reaction except for the region inside the defect. The obtained results showed that the energy barrier for two ORR mechanisms is the same order as that found for the well-known transition metal alloys.[50–52] Therefore, the reaction rate of the ORR on WTe_2^d is comparable to that on the transition metal alloys, which can be estimated by the Arrhenius formula $\sim\exp(-A_e/kT)$, where A_e is the activation energy barrier of the reaction. There is no experimental data available for the ORR on the defective WTe_2. However, by the computational study, we showed that the WTe_2 with the vacancy is a promising electrocatalyst. Therefore, we expect that the obtained results should be confirmed by experiments.

4. Conclusion

In this study, we used density functional theory calculations to search for the intermediates of oxygen reduction reaction and explore their adsorption sites on the Te vacancy WTe_2 substrate. We found that the atomic and molecular oxygen-containing intermediates occur inside and outside the Te vacancy region, respectively. Particularly, the oxygen molecule can make the transition to two oxygen atoms by overcoming an energy barrier of 0.28 eV when changing the adsorption site from above to inside the defect. Besides, the dissociative and associative mechanisms have also been examined. The mechanisms were found to proceed in a controllable manner with a moderate energy barrier of about 0.95 and 1.52 eV at the boundary and exterior of the Te defect region, respectively. However, at the interior of the vacancy, the reverse process perhaps happens and hence hinders the oxygen reduction reaction, which is due to the strong adsorption of the atomic oxygen-containing intermediates. From the obtained results, we found that the Te defect WTe_2 provides not only reactive sites but also excellent performance for the oxygen reduction reaction.

Conflicts of interest

There are no conflicts of interest to declare.

Acknowledgements

This research is funded by Ho Chi Minh City University of Technology (HCMUT), VNU-HCM, under grant number BK-SDH-2020-1770248.

References

1 A. Brouzgou, A. Podias and P. Tsiakaras, *J. Appl. Electrochem.*, 2013, **43**, 119–136.
2 E. H. Majlan, D. Rohendi, W. R. W. Daud, T. Husaini and M. A. Haque, *Renewable Sustainable Energy Rev.*, 2018, **89**, 117–134.
3 S. J. Peighambardoust, S. Rowshanzamir and M. Amjadi, *Int. J. Hydrogen Energy*, 2010, **35**, 9349–9384.
4 J.-H. Wee, *Renewable Sustainable Energy Rev.*, 2007, **11**, 1720–1738.
5 S. Walch, A. Dhanda, M. Aryanpour and H. Pitsch, *J. Phys. Chem. C*, 2008, **112**, 8464–8475.
6 E. Watanabe, H. Ushiyama and K. Yamashita, *Catal. Sci. Technol.*, 2015, **5**, 2769–2776.
7 X. Yang, A. Banerjee, Z. Xu, Z. Wang and R. Ahuja, *J. Mater. Chem. A*, 2019, **7**, 27441–27449.
8 R. Ma, G. Lin, Y. Zhou, Q. Liu, T. Zhang, G. Shan, M. Yang and J. Wang, *npj Comput. Mater.*, 2019, **5**, 78.
9 A. Sarapuu, E. Kibena-Põldsepp, M. Borghei and K. Tammeveski, *J. Mater. Chem. A*, 2018, **6**, 776–804.
10 Z. R. Ismagilov, M. A. Kerzhentsev, N. V. Shikina, A. S. Lisitsyn, L. B. Okhlopkova, Ch. N. Barnakov, M. Sakashita, T. Iijima and K. Tadokoro, *Catal. Today*, 2005, **102–103**, 58–66.

11 H. A. Gasteiger, S. S. Kacha, B. Sompalli and F. T. Wagner, *Appl. Catal., B*, 2005, **56**, 9–35.
12 X. Zhou, Y. Gan, J. Du, D. Tian, R. Zhang, C. Yang and Z. Dai, *J. Power Sources*, 2013, **232**, 310–322.
13 N. M. Markovic, T. J. Schmidt, V. Stamenkovic and P. N. Ross, *Fuel cells*, 2001, **1**, 105–116.
14 A. Qaseem, F. Chen, X. Wu and R. L. Johnston, *Catal. Sci. Technol.*, 2016, **6**, 3317–3340.
15 Y. Nie, L. Li and Z. Wei, *Chem. Soc. Rev.*, 2015, **44**, 2168–2201.
16 A. M. G. Marín, R. Rizo and J. M. Feliu, *Catal. Sci. Technol.*, 2014, **4**, 1685–1698.
17 W. Li, Z. Chen, L. Xu and Y. Yan, *J. Power Sources*, 2010, **195**, 2534–2540.
18 T. Toda, H. Igarashi, H. Uchida and M. Watanabe, *J. Electrochem. Soc.*, 1999, **146**, 3750–3756.
19 J. Liu, X. Fan, C. Sun and W. Zhu, *Materials*, 2018, **11**, 33.
20 Z. Yin, L. Lin and D. Ma, *Catal. Sci. Technol.*, 2014, **4**, 4116–4128.
21 D. Jariwala, V. K. Sangwan, L. J. Lauhon, T. J. Marks and M. C. Hersam, *ACS Nano*, 2014, **8**, 1102–1120.
22 Y. Li, Y.-L. Li, B. Sa and R. Ahuja, *Catal. Sci. Technol.*, 2017, **7**, 545–559.
23 X. Yang, A. Banerjee and R. Ahuja, *Catal. Sci. Technol.*, 2019, **9**, 4981–4989.
24 A. Eftekhari, *J. Mater. Chem. A*, 2017, **5**, 18299–18325.
25 B. Balasubramaniam, N. Singh, P. Kar, A. Tyagi, J. Prakash and R. K. Gupta, *Mol. Syst. Des. Eng.*, 2019, **4**, 804–827.
26 H. Tao, Q. Fan, T. Ma, S. Liu, H. Gysling, J. Texter, F. Guo and Z. Sun, *Prog. Mater. Sci.*, 2020, DOI: 10.1016/j.pmatsci.2020.100637.
27 S. J. Rowley-Neale, J. M. Fearn, D. A. C. Brownson, G. C. Smith, X. B. Ji and C. E. Banks, *Nanoscale*, 2016, **8**, 14767–14777.
28 S. Jayabal, G. Saranya, J. Wu, Y. Q. Liu, D. S. Geng and X. B. Meng, *J. Mater. Chem. A*, 2017, **5**, 24540–24563.
29 H. Huang, X. Feng, C. C. Du and W. B. Song, *Chem. Commun.*, 2015, **51**, 7903–7906.
30 Y. Singh, S. Back and Y. Jung, *ChemElectroChem*, 2018, **5**, 4029–4035.
31 H. Huang, X. Feng, C. C. Du, S. Y. Wu and W. B. Song, *J. Mater. Chem. A*, 2015, **3**, 16050–16056.
32 Z. X. Wang, J. X. Zhao, Q. H. Cai and F. Y. Li, *J. Mater. Chem. A*, 2017, **5**, 9842–9851.
33 H. Huang, X. Zhang, Y. Zhang, B. Huang, J. Cai and S. Lin, *Int. J. Hydrogen Energy*, 2018, **43**, 8290–8297.
34 I. S. Kwon, I. H. Kwak, J. Y. Kim, H. G. Abbas, T. T. Debela, J. Seo, M. K. Cho, J.-P. Ahn, J. Park and H. S. Kang, *Nanoscale*, 2019, **11**, 14266–14275.
35 K. Yuan, X. D. Zhuang, H. Y. Fu, G. Brunklaus, M. Forster, Y. W. Chen, *et al.*, *Angew. Chem., Int. Ed.*, 2016, **128**, 6972–6977.
36 J. H. Guo, Y. T. Shi, X. G. Bai, X. C. Wang and T. L. Ma, *J. Mater. Chem. A*, 2015, **3**, 24397–24404.
37 K. Zhao, W. Gu, L. Y. Zhao, C. L. Zhang, W. D. Peng and Y. Z. Xian, *Electrochim. Acta*, 2015, **169**, 142–149.
38 H. Liu, N. Han and J. Zhao, *RSC Adv.*, 2015, **5**, 17572–17581.
39 G. Kresse and J. Furthmüller, *Phys. Rev. B: Condens. Matter Mater. Phys.*, 1996, 11169.
40 J. P. Perdew, J. A. Chevary, S. H. Vosko, K. A. Jackson, M. R. Pederson, D. J. Singh and C. Fiolhais, *Phys. Rev. B: Condens. Matter Mater. Phys.*, 1992, **46**, 6671–6687.
41 J. P. Perdew, K. Burke and M. Ernzerhof, *Phys. Rev. Lett.*, 1996, **77**, 3865–3868.
42 P. E. Blöchl, *Phys. Rev. B: Condens. Matter Mater. Phys.*, 1994, **50**, 17953–17979.
43 G. Kresse and D. Joubert, *Phys. Rev. B: Condens. Matter Mater. Phys.*, 1999, **59**, 1758–1775.
44 P. E. Blöchl, C. J. Först and J. Schimpl, *Bull. Mater. Sci.*, 2003, **26**, 33–41.
45 H. J. Monkhorst and J. D. Pack, *Phys. Rev. B: Condens. Matter Mater. Phys.*, 1976, **13**, 5188–5192.
46 H. Jónsson, G. Mills and K. W. Jacobsen, in *Classical and quantum dynamics in condensed phase simulation*, World Scientific, Singapore, 1998, pp. 385–404.
47 G. Henkelman, B. P. Uberuaga and H. Jónsson, *J. Chem. Phys.*, 2000, **113**, 9901–9904.
48 G. Henkelman and H. Jónsson, *J. Chem. Phys.*, 2000, **113**, 9978–9985.
49 J. K. Nørskov, J. Rossmeisl, A. Logadottir, L. Lindqvist, J. R. Kitchin, T. Bligaard and H. Jonsson, *J. Phys. Chem. B*, 2004, **108**, 17886–17892.
50 D. N. Son and K. Takahashi, *J. Phys. Chem. C*, 2012, **116**, 6200–6207.
51 D. N. Son, O. K. Le, V. Chihaia and K. Takahashi, *J. Phys. Chem. C*, 2015, **119**, 24364–24372.
52 D. N. Son, P. N. Thanh, N. D. Quang, K. Takahashi and M. P. Pham-Ho, *J. Appl. Electrochem.*, 2017, **47**, 747–754.